RESEARCH ARTICLES

Polarization-Modulated Smectic Liquid Crystal Phases

D. A. Coleman,[1] J. Fernsler,[1] N. Chattham,[1] M. Nakata,[2] Y. Takanishi,[2] E. Körblova,[3] D. R. Link,[1,2] R.-F. Shao,[1] W. G. Jang,[1] J. E. Maclennan,[1] O. Mondainn-Monval,[4,5] C. Boyer,[4] W. Weissflog,[6] G. Pelzl,[6] L.-C. Chien,[7] J. Zasadzinski,[4] J. Watanabe,[2] D. M. Walba,[3] H. Takezoe,[2] N. A. Clark[1]*

Any polar-ordered material with a spatially uniform polarization field is internally frustrated: The symmetry-required local preference for polarization is to be nonuniform, i.e., to be locally bouquet-like or "splayed." However, it is impossible to achieve splay of a preferred sign everywhere in space unless appropriate defects are introduced into the field. Typically, in materials like ferroelectric crystals or liquid crystals, such defects are not thermally stable, so that the local preference is globally frustrated and the polarization field remains uniform. Here, we report a class of fluid polar smectic liquid crystals in which local splay prevails in the form of periodic supermolecular-scale polarization modulation stripes coupled to layer undulation waves. The polar domains are locally chiral, and organized into patterns of alternating handedness and polarity. The fluid-layer undulations enable an extraordinary menagerie of filament and planar structures that identify such phases.

The discovery that polar order (*1*) and macroscopic chirality (*2*) appear spontaneously in fluid smectic liquid crystals (LCs) of achiral bent-core "bow" or "banana-shaped" molecules as a result of distinct broken orientational symmetries opened the study of a broad new class of polar condensed phases of unexpected richness, deriving from the interplay of polarity and chirality (*3*). The four basic polar chiral smectic banana phases (the SmCPs or B2s) are layered, either with the same tilt in adjacent two-dimensional (2D)–fluid layers (synclinic, C_S) or with opposite tilt in adjacent layers (anticlinic, C_A), and either synpolar (ferroelectric, P_F) or antipolar (antiferroelectric, P_A), as sketched in Fig. 1A, where chirality (handedness) is indicated by color (magenta versus cyan). All four of these B2 subphases have been found in materials of bent-core molecular family shown in Fig. 1A: the SmC_SP_A (racemic antiferroelectric) and SmC_AP_A (homochiral antiferroelectric) structures in the prototypical material NOBOW (*2*, *4*); and the SmC_AP_F (racemic ferroelectric) in a material not shown here (*5*). Several other materials, including MHOBOW (*6*, *7*), PBCOB (*8*), H87 (*9*), and CITRO (*10*) in Fig. 1 exhibit the SmC_SP_F (homochiral ferroelectric) structure, but under heretofore mysterious circumstances: SmC_SP_F characteristics appear only if a suitably large electric field is applied, and then only irreversibly from equilibrium states of unknown structure that are so different from the other B2s that they have until now been grouped as separate phases, the B7 class (*11*).

Upon cooling from the isotropic, B7 phases grow in a wildly variegated morphology of domains that are unusually beautiful even by LC standards (see cover), featuring twisted helical filaments (*6*, *8*, *12*–*14*) (Fig. 2, A and B), high- and low-birefringence focal conics striped either parallel or normal to the smectic layering (*12*, *15*) (Fig. 2C), banana leaf–shaped domains (*15*) (Figs. 3E and 4), checkerboard textures (*6*, *12*, *14*–*16*) (Fig. 2C), and freely suspended filaments (*12*, *16*, *17*). We combine x-ray diffraction (XRD), freeze fracture transmission electron microscopy (FFTEM), and depolarized transmission and reflection light microscopy (DTLM and DRLM) to establish unambiguously the underlying structural principle of the B7 phases. In so doing, we find yet another exotic broken symmetry, the spontaneous periodic modulation of the polarization density into splay domains. We thus establish the existence of a new class of bulk condensed phases, which join the vortex lattice (*18*), twist grain boundary (*19*), and blue (*20*) phases as periodic structures stabilized by a free-energy term linear in a field gradient.

In polar fluid LCs such as the SmCPs, the polarization **P** is free to rotate continuously in the layer plane in response to surface, electric, and elastic torques (i.e., its orientation is a Goldstone variable, in contrast to solid ferroelectrics, where **P** adopts a set of discrete orientations established by a lattice). A consequence of this orientational freedom is the possibility of polarization modulation (PM), an example of which is shown in Fig. 1B. Because of its vectorial symmetry, the local energy density of the **P** field contains a term of the form $U \sim (\nabla \bullet \mathbf{P} - c_o)^2$, where c_o is a constant, stabilizing finite splay of **P** (e.g., c_o, $\nabla \bullet \mathbf{P} > 0$ in the red example of Fig. 1B) (*21*). However, filling space such that the volume average $\langle \nabla \bullet \mathbf{P} \rangle \neq 0$, requires spatial inhomogeneity, such as the stripes sketched in Fig. 1C, where the regions with $\nabla \bullet \mathbf{P} < 0$ are confined to less well-ordered defect lines (green). In known ferroelectrics such defects are too costly in energy, so **P** reverts to its uniform state and the tendency for local splay is globally frustrated (*22*). PM has been proposed and observed to date in a variety of LC interfacial structures, such as freely suspended smectic films (*23*–*30*), Langmuir monolayers (*31*, *32*) and phospholipid tubules (*33*), and has been proposed to explain undulated lamellar lipid phases (*34*) and analog chiral smectic electro-optic (EO) behavior (*35*). Here, we demonstrate the existence of bulk phases with polarization modulation stabilized by polarization splay.

Based on the results we present below, we will propose that the B7 is a polarization modulated/undulated layer (PM/UL) stripe structure. In a SmCP system, the molecular bananas reorient across splay stripes in four combinations of handedness and orientation of **P** for a given sign of splay, as shown in Fig. 1D. The essential feature establishing the relation between the polarization modulation and the layer undulations is illustrated in Fig. 1E: Along the PM defect lines, the layers are necessarily thicker because the disorder in both **P** and molecular azimuthal orientation (at the green boundaries in Fig. 1D) will produce a smaller molecular tilt. In a bulk material, the pitch of the layering along **s** must be the same everywhere, requiring the thinner layer regions between the defect lines to tilt and effectively thicken along the mean **s**, as they do, for example, in the formation of the smectic chevron structure (*36*) and the smectic undulation instability (*37*). The result

[1]Department of Physics and Ferroelectric Liquid Crystal Materials Research Center, University of Colorado, Boulder, CO 80309–0390, USA. [2]Department of Organic and Polymeric Materials, Tokyo Institute of Technology O-okayama, Meguro-ku, Tokyo 152-8552, Japan. [3]Department of Chemistry and Biochemistry and Ferroelectric Liquid Crystal Materials Research Center, University of Colorado, Boulder, CO 80309–0215, USA. [4]Department of Chemical Engineering, University of California, Santa Barbara, CA 93106, USA. [5]Centre de Recherche Paul Pascal–CNRS, Av. A. Schweitzer, 33 600 Pessac, France. [6]Institut für Physikalische Chemie, Martin-Luther-Universität D-06108 Halle, Muehlpforte 1, Germany. [7]Liquid Crystal Institute, Department of Chemical Physics, Kent State University, Kent, OH 44242, USA.

*To whom correspondence should be addressed. E-mail: noel.clark@colorado.edu

is an undulated PM structure having a pitch (distance along **s** per layer) d_s that is larger than d, the pitch of the flat, defect-free layers, as is observed (Fig. 3D).

B7 layer structure. Synchrotron-based powder and single-domain microbeam XRD data (*38*, *39*) and FFTEM observations provide basic evidence for a generic structure for the B7 phases. Previous XRD studies of B7 phases have found a diffuse peak at high angle, which indicates that the layers are 2D fluids. Additional small angle peaks indicate complexity beyond a simple lamellar structure and suggest 2D ordering (*12*, *15*, *40*–*42*). Our powder scans for MHOBOW and PBCOB in Fig. 3, A and B, typical of the blue-labeled B7s in Fig. 1, indeed show 2D ordering, with three distinct features: a series of peaks at very small angle, and closely spaced sets of multiple peaks, previously unresolved, near scattering vectors $\mathbf{q} \sim 0.16$ Å^{-1} (Fig. 3A; s = 1) and $\mathbf{q} \sim 0.33$Å^{-1} (Fig. 3B; s = 2), where the single-peak lamellar reflections would appear for simple lamellar SmCP phases (fig. S1). This powder pattern is accurately indexed by the rectangular 2D reciprocal lattice indicated in the inset in Fig. 3A, with indices [s,m] on the basis vector set $\boldsymbol{\kappa}_s = \mathbf{s}(2\pi/d_s)$ in the mean layer normal direction, **s**, and $\boldsymbol{\kappa}_m = \mathbf{m}(2\pi/d_m)$, a much smaller fundamental (in-layer) wavevector, with an angle $\beta = 90°$ between **s** and **m**. H87, qualitatively identical in its scattering signature, has the largest d_m of the B7s studied here (fig. S2).

Quantitative analysis of the intensities of these peaks follows from assuming the electron density to be that of periodically undulated layers, i.e., $\rho(\mathbf{r}) = \Sigma_n f\{z - [nd + u_n(\mathbf{r})]\}$, where d is the intrinsic smectic layer thickness, $f\{z\}$ is the layer electron density profile of a single layer, and $u(\mathbf{r}) = \Sigma_j A_j \cos(j\mathbf{k}_m \bullet \mathbf{r})$ is the periodic local layer displacement along **s** (*43*). The relative MHOBOW intensities I(s,m) for s = 1 in Fig. 3A and s = 2 in Fig. 3B can be fit quite well with the further assumption that the undulation is simply sinusoidal, i.e., with only $A_1 \neq 0$, as indicated in Fig. 3C (*44*). These and the data on the other B7s thus indicate a structure of stacked smectic layers, periodically undulated with wavelength d_m as follows: MHOBOW {d = 38.8 Å, A_1 = 11 Å at T = 139°C, (274 Å at 139°C) < d_m < (349 Å at 100°C)} (fig. S1); PBCOB {d_m = 286 Å at T = 110°C}; H87 {(450 Å at 158°C) < d_m < (700 Å at 135°C)} (fig. S2); and CITRO {d_m = 153 Å at T = 100°C} (*45*). An interesting feature of the simple undulation model is that it predicts zero intensity for s = 0, i.e., absence of the zero-order reflections shown in Fig. 3B. Thus, these peaks must originate from structural features internal to the layers, e.g., electron density modulation associated with the splay defect lines.

X-ray microdiffraction with a 5-μm-diameter beam was carried out on single CITRO nested cylinder focal conic domains (FCDs) (Fig. 3D) and MHOBOW "banana leaf" domains (BLDs) (Figs. 3E and 4), prominent textural features of B7 phases as grown by cooling from the isotropic with the LC filling the gap of a cell made by spacing two plates a few micrometers apart (*38*). Figure 3E illustrates the BLD experiment with the beam passing through the BLD within the yellow circle. This experiment revealed the **q**-space orientation of the BLDs indicated in Fig. 3E, with the mean layer normal **s** parallel to both the glass and to the leaf long axis, and the undulation wavevector **m** normal to the glass, and yielded an s = 1 **q**-space structure that is fully consistent with the powder results of Fig. 3C. The $I(\mathbf{q}_m)$ versus $\mathbf{q}_m$ scan in Fig. 3E is at $\mathbf{q}_s = 2\pi/d_s$ (s = 1, essentially rocking the sample about the **p** axis with $\mathbf{q}_s = 2\pi/d_s$) and shows the s = 1, m = 0, ±1, and ±2 reflections of the undulation lattice with amplitude ratios in good agreement with those of

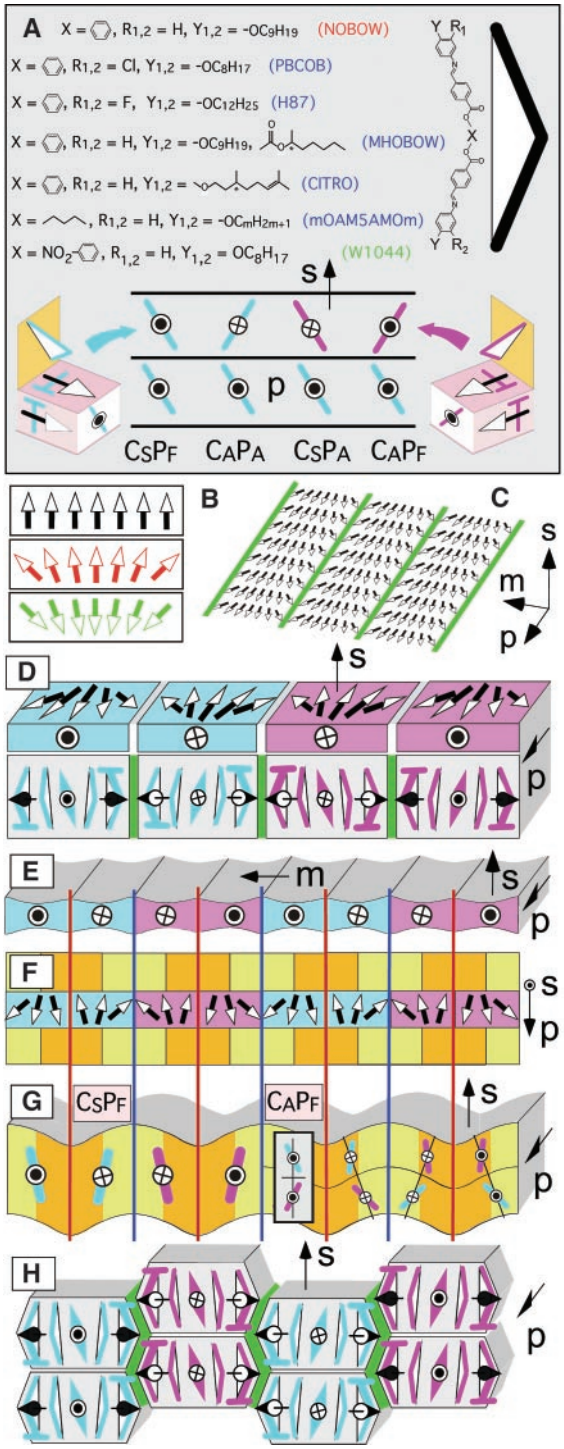

Fig. 1. (**A**) The B7 materials studied here (blue labels) are homologs of the prototypical SmCP (B2) NOBOW. The SmCP smectic layer structure has spontaneous polar order and tilt of the bows, which makes the layers chiral, with handedness indicated by color (cyan or magenta), and gives the four possible bilayer phases shown, all of which have been observed. Tees () indicate the projection of bow-string orientation, with the bar indicating the end nearest the reader. We show here that the B7 textures are a feature only of the SmC_SP_F. (**B**) Preferred structure of a polarization field will be either positive (red) or negative (green) splay. (**C**) Stripes assuming positive splay can fill space if the required defects (green lines) are sufficiently low in energy. (**D**) Elemental splay stripe varieties, depending on handedness and on orientation of **P**. The absolute sign of the polarization splay is unknown at present. For consistency in the B7 sketches, we draw the polarization splay with the bent-core vertex splayed out. However, it may be the other way around. The tees indicate tilt of the molecule toward the reader. (**E**) The basic undulation-driving mechanism is layer expansion at the splay defect lines. (**F** and **G**) The layers in the intermediate regions must tilt to establish a uniform layer pitch along **s**. This organization of **P**, chirality, and undulation [yellow (orange) displaced up (down)] is inferred from the optical and x-ray experiments. There are two distinct kinds of defect lines: those where handedness changes (blue), and those where it does not (red), making the undulation crest curvature different from that of the troughs. (G) Director strain, minimized in the undulated synclinic (C_S) local structure, tends to suppress the undulation in the anticlinic (C_A) structure. (**H**) Layer interdigitation provides effective molecular packing at the polarization splay defects to produce a distinct (B1) family of 2D ordered phases.

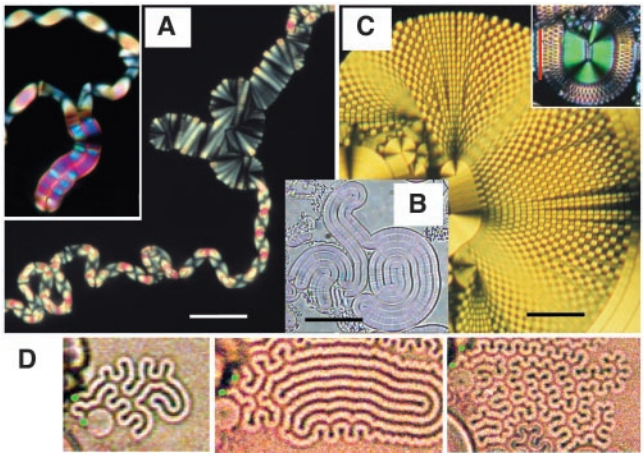

Fig. 2. Typical textures of MHOBOW in the B7 phase viewed in DTLM, showing (**A**) helical filaments grown in from the isotropic phase and trapped on the surface to form 2D FCDs; (**B**) surface trapped filament folding on the surface as it grows to form a 2D FCD; (**C**) a checkerboard texture in a 4-μm-thick cell and an FCD (inset) in a 6-μm-thick cell; and (**D**) growth upon cooling of a MHOBOW filament tethered to the surface. The spontaneously undulated filament packs into local arrangements that can be checkerboard or stripe-like. Scales: (A), 100 μm; (B), 100 μm; (C), 80 μm (inset, 100 μm); and (D) circular domain, 50 μm in diameter.

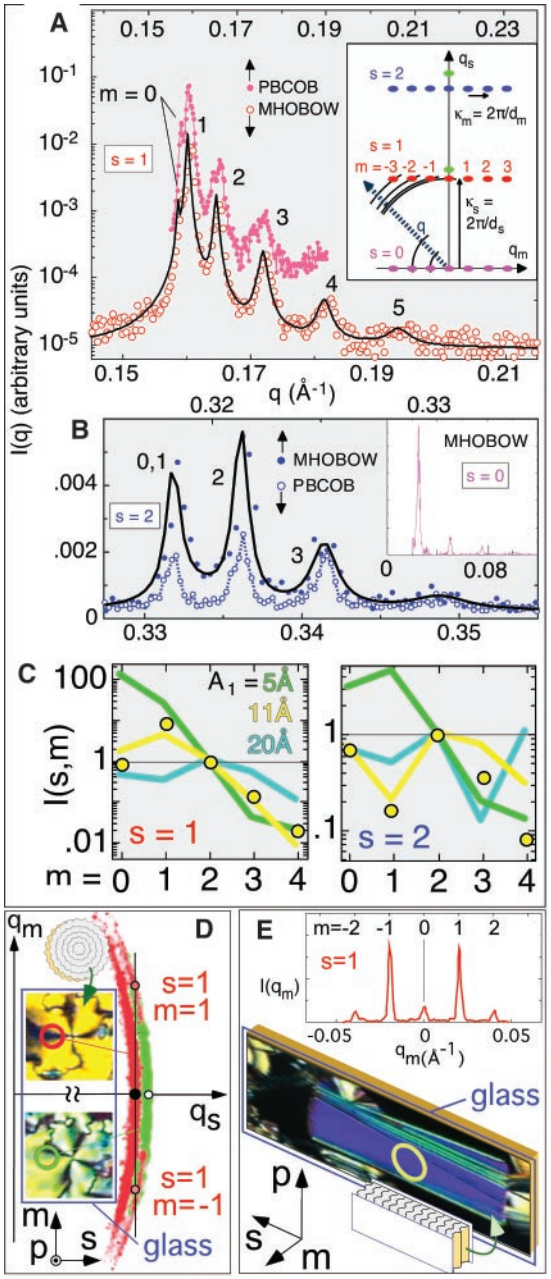

Fig. 3. (**A** and **B**) Powder x-ray structure factor $I(\mathbf{q})$ of B7 MHOBOW at T = 131°C and the fit to a set of peaks (black line) constrained in position by the 2D rectangular lattice in the inset of (A). The PBOCB B7 data (T = 110°C) can be similarly fit. (**C**) Relative integrated intensities $I(\mathbf{s},\mathbf{m})$ of the MHOBOW peaks of (A) and (B) with $I(s, 2)$ scaled to 1 (open circles), and predictions of the layer undulation model with undulation amplitude A_1 as a parameter (solid lines). The model, quite sensitive to A_1, fits best for A_1 = 11 Å for MHOBOW. (**D**) Area detector image of x-ray scattering intensity $I(\mathbf{q}_m,\mathbf{q}_s)$ with the microbeam illumination within the circled area of a CITRO FCD at T = 100°C, before (red) and after (green) electric field application (imaged area 150 μm^2). Before the field the s = 1, m = ±1 reflections with d_s = 36.3 Å and d_m = 153 Å appear (red), showing that in the FCD **s** and **m** are parallel to the glass plates, as sketched. Field application yields an $I(\mathbf{q}_m,\mathbf{q}_s)$ having a single lamellar reflection (green) at a larger $\mathbf{q}_s$, evidence for the layer flattening and contraction produced by the field elimination of the PM and its undulation. Under this condition brush rotation, characteristic of the chiral ferroelectric SmC_sP_F, is observed (green). The shift in $\mathbf{q}_s$ indicates that the maximum undulation slope is 14.5°, which gives A_1 = 6.0 Å in CITRO. (**E**) DTLM image of a 200-μm-long MHOBOW banana leaf domain (BLD), along with x-ray scattered intensity $I(\mathbf{q}_m)$ at $\mathbf{q}_s = 2\pi/d_s$ (s = 1) from microbeam illumination through a 5-μm-diameter area (inside yellow circle) of a MHOBOW BLD. $I(\mathbf{q}_s,\mathbf{q}_m)$ shows that **s** is parallel to the BLD long axis and that **m** is normal to the plates, as sketched. The peak positions (giving d_m = 330 Å) and intensities agree well with the powder data and undulation model predictions in (C).

Fig. 3C. Thus, the overall layer structure of the BLD, sketched in Fig. 4C, is "bookshelf," with the layers on-average normal to the plates and the undulation crests and troughs parallel to the glass. Figure 3D shows microbeam scattering from the pictured FCD of B7 CITRO. With x-rays incident on an FCD grown by cooling from the isotropic phase (through the red circle and nearly normal to the glass), the red-shaded scattering is observed, the [s = 1, m = 0, ±1] reflections (pink dots) indicating that the undulated layers are oriented as indicated, with both **s** and **m** parallel to the glass plates (plane of the page). The scattering is in arcs here because of the large mosaic spread due to the curvature of the layers in the nested cylinder structure of the FCD.

Freeze fracture was carried out by quenching the LC, sandwiched between 2 mm by 2 mm Cu planchettes, from various temperatures in the B7 range to 77 K by rapid immersion in liquid nitrogen or propane, and fracturing cold in a vacuum. FFTEM of Pt-C fracture face replicas revealed topographies having the global structure of single- and multiple-layer steps familiar from the study of fluid thermotropic and lyotropic smectics (*46*, *47*). However, the layers that would appear flat and smooth for such materials were, in MHOBOW, distinctly marked by a 1D periodic pattern of layer undulations (ripples) of supermolecular wavelength d_m [$d_m \sim$ 500 Å in the example of Fig. 5A, quenched from T = 120°C (*45*)]. The single-layer step shown in Fig. 5A reveals directly the undulation, and the multiple-step "cliffs" in Fig. 5, A and B, show it to propagate through many layers unchanged in structure. This structure is qualitatively consistent with that extracted from the x-ray results, and, given the typical uncertainty in FFTEM scales, the d_m's are in reasonable agreement with the x-ray values. The ripples in Fig. 5 appear to be mirror symmetric about the planes of layer displacement maxima and minima, justifying the cosine expansion of $u(\mathbf{r})$. However, they exhibit distinct textural domains (Fig. 5B) that indicate (i) a lack of glide symmetry of the undulation for half-period displacement along **m**, the direction of the undulation wavevector and reflection about the plane of zero-layer displacement (i.e., the crests are rounded while the valleys are sharp, or vice versa, Fig. 5B); and (**ii**) an orthogonal lattice structure because the mean layer orientation is the same in the two domains. Such a layer structure is on average polar (along the layer normal, **s**) (*48*, *49*).

Visualizing the polarization modulation. The chemical stability of NOBOW and its B7 analogs in Fig. 1A is limited because of the susceptibility of these molecules to hydrolysis, which splits them in two at their Schiff's-base (CHN) linkages. This effect

produces a decrease of the isotropic-B7 transition temperatures with x-ray exposure and aging at temperature and, as found in the XRD and FFTEM experiments, an increase of undulation wavelength with aging, with d_m growing to at least 600 Å in bulk MHOBOW. This effect, although a nuisance, permits direct optical microscopic observation of the molecular orientation/polarization modulation patterns, because d_m was found to increase with aging well into the micrometer range in freely suspended films of MHOBOW (*50*), and both thermally and with aging in freely suspended films of mOAM5AMOm (*51*) (**m** = 8, 12, 14, 16) (*52*). Films that were 2 to 10 layers thick (i.e., with **s** normal to the film plane) were freely suspended in air (*53*) by drawing them in the B7 phase over a 5-mm-diameter hole in a glass cover slip (*54*) and then imaged with DRLM (*55*). Freshly made MHOBOW films exhibited a 2D focal conic (FC) texture of orientation of the in-plane optic-axis projection (Fig. 6A), which remained unchanged with application of small in-plane field (**E** ~ 100 V/cm). Upon aging over several days at T = 144°C, a gradually coarsening stripe pattern (indicating increasing d_m) appeared on the FCs (Fig. 6B), which finally evolved to distinct defect lines (Fig. 6C) where the bend (splay) deformation of the in-plane orientation of the tilted optic axis (of the polarization) abruptly changes sign. This texture is locally SmC_SP_F, responding as a tilted chiral smectic to an applied in-plane field (*53*) and, like NOBOW, has a larger in-plane refractive index for optical polarization along **p** (Fig. 2A). Because **s** must be normal to the image-film-layer plane, the initial 2D FC is direct evidence that the texture of (**m**,**p**) is 1D smectic-like, i.e., stripes in the layer plane with a pitch too small to resolve optically, mapping onto the 2D FC as shown in Fig. 6A. DRLM of the FCs shows in-plane optical anisotropy with higher refractive index for polarization parallel to these stripes and thus to the polarization direction **p**, as expected for the PM structures sketched in Fig. 1C, confirming the mapping of (**m**, **p**). Identical 2D focal conic textures and coarsening with aging were found in B7 films of the mOAM5AMOm series, with the key additional observation that in this system coarsening to the splay stripe textures could also be induced immediately simply by cooling to the low end of the B7 phase (Fig. 6F). These 2D FC textures in the films are similar to, and have the same sign of optical anisotropy as, the low-birefringence FC domains grown from the isotropic in the glass cells (Fig. 6D), indicating that the latter domains have the same geometry—i.e., are homeotropic—with **s** normal to the glass/image plane. The orientation pattern in Fig. 6C, identical to that found in polarization-modulated SmC films (*30*), is mapped in Fig. 6E, showing the splay of **P**(**r**) and the line defects that enable it. PM states found to date in films are bistripe, i.e., we have not observed the four-stripe bulk MHOBOW structure (Figs. 1F and 4C) in large-period film PM. These film observations likely explain the periodic free surface undulations found by atomic force microscopy of B7 preparations (*56*).

The PM/UL state. Simple theoretical considerations impose additional constraints on the layer organization of a PM state: (i) Stripe domains in SmCP layers come in the four varieties of Fig. 2C, depending on the relative orientation of **P** and the handedness of the molecular tilt. However, in the PM/UL structure these must be such that the tilt is synclinic (C_S), as in Fig. 1G, with the tilt plane orientation compensating the undulation to reduce elastic strain in each layer. As Fig. 1G shows, anticlinic (C_A) layering leads to large elastic deformation in alternate layers that suppresses the modulation. (ii) PM will not be observed in any antiferroelectric SmCP, because alternation in sign of the polarization splay from layer to layer removes the basic driving force for global splay of **P**. Thus, strong evidence that polarization splay drives PM is provided by our key observation that among known SmCPs, the PM/UL state is a feature of only the SmC_SP_F variety of Fig. 1A (*57*). Next, we consider the overall arrangement of the P-splay stripes, which may depend on the material and may even be different in a different domain of a given material. Thus, antiferroelectric order-

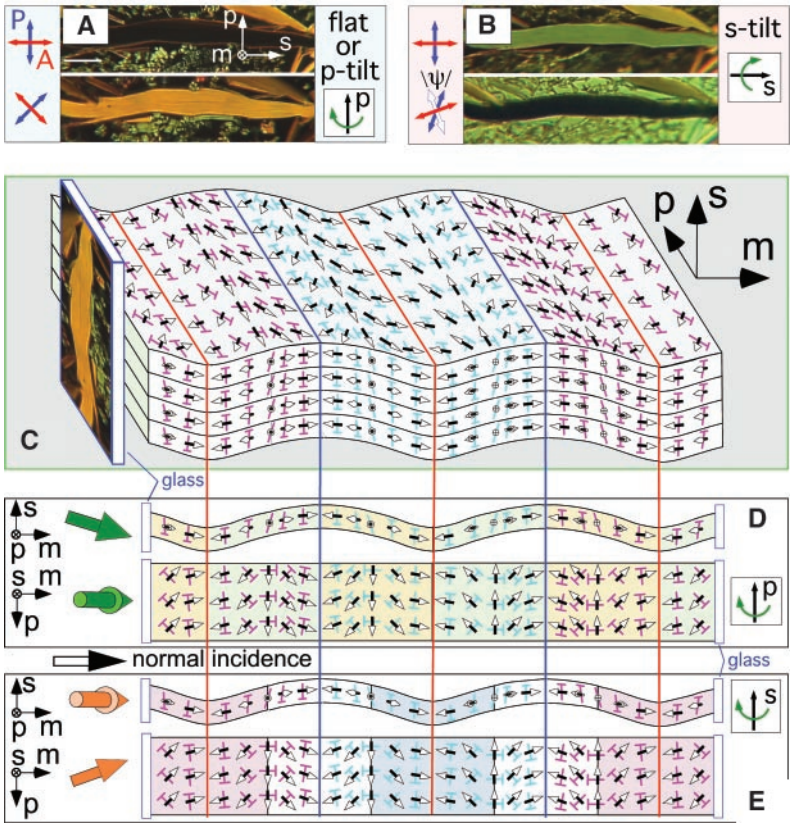

Fig. 4. Transmission polarized light micrographs of a 4-μm-thick MHOBOW B7 BLD showing the optical effects of oblique incidence obtained by tilting the sample. The orientation of the **s**-**m**-**p** triad is inferred from the microbeam x-ray of Fig. 3E. (**A**) At normal incidence (sample flat), the leaf is birefringent and achiral, extinguishing between crossed polarizer (blue)/analyzer oriented parallel or normal to the long axis, and transmitting otherwise. Tilting around the BLD short axis (**p**) produces no change in this. Scale bar, 50 μm. (**B**) Remarkably, upon tilting around the BLD long axis (**s**) the domain becomes optically chiral, extinguishing the exiting light (white arrow), with polarizer and analyzer uncrossed as indicated. The angle of the optical polarization rotation, ψ, is proportional to the sample tilt. (**C**) Structure of a MHOBOW BLD [along with photo of Fig. 4B in perspective] as inferred from the x-ray, freeze fracture, and optical data. The structure shows the PM stripe undulation, alternation of polarity and chirality, and two distinct types of PM defect lines (red, blue). (**D** and **E**) Top and side views of the PM structure, with green (orange) arrows indicating incident light with the cell tilted about **p**,**s** as in (A) and (B), respectively. Inspection shows that at normal incidence stripes of opposite chirality have identical response, giving overall achiral optics. This is also the case in (D), for sample tilt around **p**, where, although orange and gray-green shaded regions become optically nondegenerate upon tilt, each is independently on-average achiral. However, in (E), for sample tilt around **s**, the pink and gray shaded stripes become optically nondegenerate and are of opposite chirality, leading to the optical rotation shown in (B).

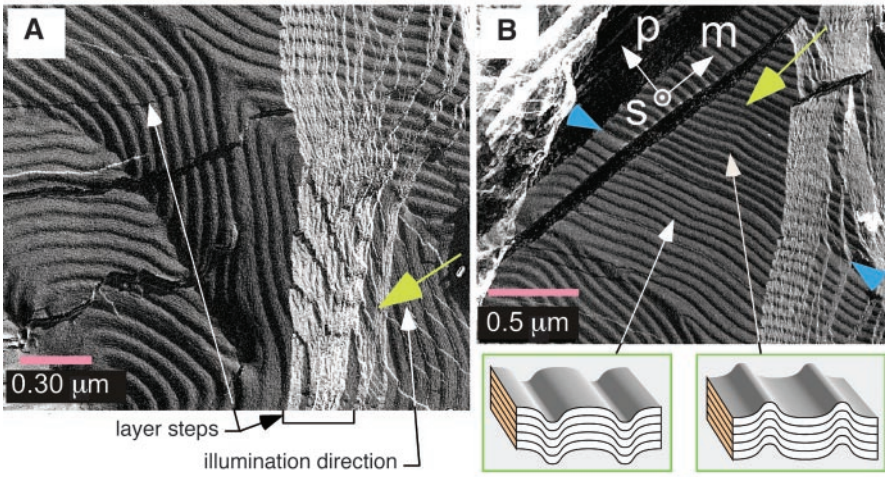

Fig. 5. (**A** and **B**) FFTEM images of a Pt-C replica shadowing the topography of a surface of a MHOBOW sample quenched from the B7 phase (T = 115°C) and fractured. Surface topography is such that darker areas would be shadowed with oblique illumination coming in the direction of the yellow arrows. The smectic fracture surfaces exhibit the usual single-layer steps, but also exhibit an atypical bulk coherent periodic undulation of wavelength $d_m \sim 500$ Å. The lines where the undulation abruptly changes direction are suggestive of FCDs in their 1D periodic order. (B) The undulation troughs and crests are not mirror symmetric, as evidenced by domain walls (blue arrows), which separate domains of opposite net polarity along **s**. The coplanarity of the layers in these two domains is indicative of a rectangular lattice. A detailed sketch of the undulated structure in shown in Fig. 4C.

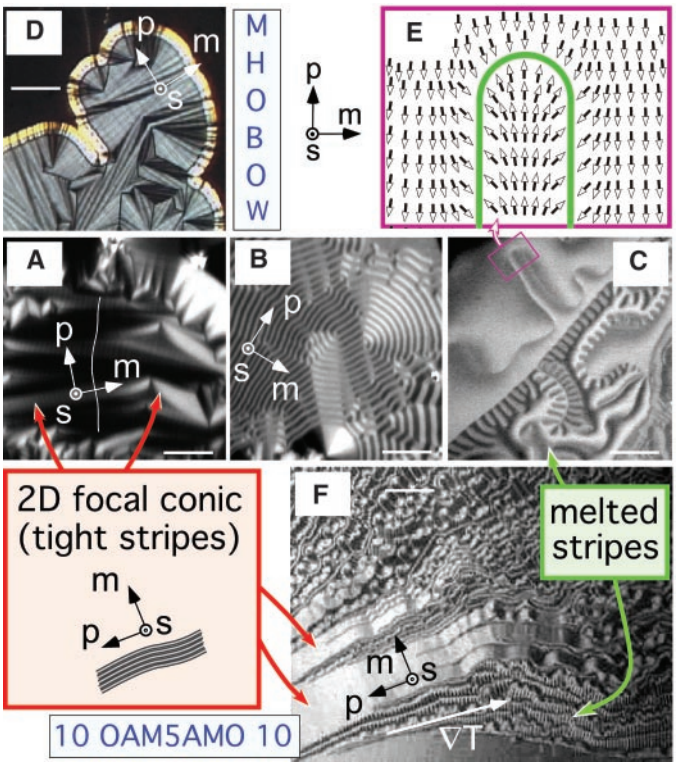

Fig. 6. Optical photomicrographs of B7 preparations having the smectic layers parallel to the plane of the image (with **s** normal to the image plane), from (**A** to **C**) an 8-layer-thick MHOBOW freely suspended film; (**D**) a 4-μm-thick homeotropic of MHOBOW sample between between glass; and (F) a ~10-layer-thick 10OAM5AMO10 film. The fresh films (A) and bulk (D) of MHOBOW show a low birefringence 2D focal conic texture [dark sample area surrounded by bright outline in (D)], evidence for the smectic-like organization of the PM, each stripe [white line in (A)] behaving as a 1D layer in the 2D smectic planes. In the film, the PM period increases with time until, after 1 day, it is visible optically (B), and after several days increases to reveal the polarization modulation stripes (C). (**E**) Mapping of **p** in the PM defect loop in (C). Identical structures have been observed in other PM film and interfacial systems (*30*). (D) B7 drop surrounded by isotropic (black area), showing a low-birefringence interior with **s** normal to the page and a bright outline with **s** parallel to the glass, bulk 3D smectic focal conic as in Fig. 3D. Scale bars: (A) to (C) and (F), 100 μm; (D), 60 μm. (**F**) 10OAM5AMO10 in a temperature gradient (cooler on the right) showing the increase of d_m and the melting of the PM lattice with decreasing T.

ing accounts for the absence of second-harmonic generation in the as-grown steady states of MHOBOW and CITRO (*10*), and the antiferroelectric racemic arrangement of P-splay domains (monostripe alternation in **P**, bistripe alternation in handedness), shown in Fig. 1, E to G, uniquely accounts for the optical properties of banana leaf domains, as discussed below. Further evidence for this picture is found in chiral MHOBOW: In a chiral material (Fig. 1), the neighboring (opposite handedness) undulation periods are no longer enantiomeric and thus should have different mean layer spacings, resulting in a weak distortion to an oblique lattice. The (S)-MHOBOW lattice is indeed found to be identical in dimension to that of racemic MHOBOW but slightly oblique (fig. S3), with an angle of $\beta = 88.2° \pm 0.2°$ between $\boldsymbol{\kappa}_s$ and $\boldsymbol{\kappa}_m$ at T = 131°C (*43*).

Electric-field expulsion of the polarization modulation. Further evidence for the PM state comes from features of the response of the B7s to an applied electric field **E**, with the LC as the dielectric in indium oxide–on–glass transparent capacitors: (i) For low fields, the coupled polarization and molecular orientation are constrained by the modulation structure, and only a weak electro-optical (EO) response is expected or found. (ii) Nonzero **E** raises the internal energy of the PM, which is then expelled in favor of a state of uniform **P** for **E** above a threshold $\mathbf{E}_{th}$, i.e., a B7-to-SmC_SP_F transition is induced. A simple (over)estimate of $\mathbf{E}_{th}$ can be obtained by equating the electric energy density with the elastic energy density of the PM: $\mathbf{PE}_{th} \sim K/d_m^2$, where $K \sim 9$ pN is the elastic constant for tilt plane reorientation (*58*), predicting $\mathbf{E}_{th} \sim 30$ V/μm for a typical B2, with $\mathbf{P}$ = 300 nC/cm^2 and d_m = 30 nm. This field-induced B7-to-SmC_SP_F phase change was observed as an irreversible, first-order transition (*59*) in all B7s studied, with $\mathbf{E}_{th}$ in the range 1 V/μm $< \mathbf{E}_{th} <$ 20 V/μm. Above threshold, the complex maze of as-grown B7 focal conic, banana leaf, homeotropic, and checkerboard domains gives way to a homogeneous texture of simple tilted smectic homochiral ferroelectric SmC_SP_F focal conics, with their unmistakable chiral EO response, described in detail for MHOBOW in (*6*). The threshold for the field-induced B7-SmC_SP_F transition in H87 has been found to decrease as the temperature T_{B7CP} of the thermal B7-SmCP transition is approached (*9*). Because d_m increases from 450 to 700Å through the B7 range as T approaches T_{B7CP}, the predicted inverse relation between $\mathbf{E}_{th}$ and d_m is qualitatively confirmed.

Combined EO and XRD evidence that **E**-induced elimination of the PM also expels the layer undulation is presented in Fig. 3D, which shows optical micrographs and microbeam scattering from FCDs of

CITRO at $T = 100°C$ in the B7 phase, as-grown (red scattering, discussed above) and **E**-modified (green scattering). Below a threshold field, neither the optical nor the x-ray data are modified by the field, but for $\mathbf{E} > 20$ V/μm, the domain begins to exhibit the chiral extinction brush rotation shown, a signature of the transition to the PM-free SmC_SP_F state (*6*), and the accompanying transition from the red- to green-shaded scattering is observed with x-ray illumination through the same region (in the red/green circles). The green scattering is a single peak centered at $\mathbf{q}_m = 0$ and shifted out relative to the red to the point indicated by ○ on the $\mathbf{q}_s$ axis, indicative of simple planar layers with a spacing d that is smaller than the pitch d_s along **s** with the undulation present. Thus, the elimination of the PM defects enables the layers to become thinner at the crests and troughs. The consequent reduction of the undulation amplitude requires the layering pitch along **s** to become equally thinner at the regions of maximum slope, approaching the PM-free layer thickness d as the slope is reduced to zero. The peak positions show that in CITRO, the maximum slope in the undulation is $\beta_{max} = 14.5°$, and thus the fractional layer expansion $\delta d/d$ at the crests and troughs is $\delta d/d = [\cos(\beta_{max})]^{-1} = 3.3\%$. A fascinating aspect of the field experiments is that even though the SmC_SP_F layering is on average racemic in the PM stripes of Figs. 2 and 4, the macroscopic SmC_SP_F state that results upon undoing the PM is homochiral (*6*, *10*, *40*).

Achiral/chiral optics of the banana leaf domains. The orientation of the **s**-**m**-**p** lattice obtained from the x-ray data on BLDs enables a definitive interpretation of their optical properties and detailed insight into the nature of the PM in MHOBOW. The key transmission polarized light microscopic observations are shown in Fig. 4, A and B, and interpreted in Fig. 1, D to F, and Fig. 4, C to E. With normal incidence, the banana leaf appears achiral and birefringent with optic axes along **s** and **p**, and remains so if the sample is tilted about **p**, the BLD short axis. Remarkably, chiral optical rotation of amplitude linear in the tilt angle ψ appears for tilting the sample about **s** (the off-diagonal dielectric tensor element $\varepsilon_{sp} \propto i\psi$). These observations put strict constraints on the possible internal organization of BLD polarity, chirality, and undulation symmetry. Because optical rotation disappears at normal incidence, the overall structure must be on average achiral, i.e., with left- and right-handed stripes related by glide reflections. Because tilting about **p** renders only the regions of differing sign of undulation slope inequivalent (Fig. 4D), the absence of optical rotation upon **p**-tilt implies that the regions of each sign of slope must be independently on average achiral. This indicates that **s**-**m** is the glide plane, requiring then that the overall structure be antiferroelectric with a period of two undulation wavelengths. It then remains only to choose between two possibilities for the alternation in handedness in the stripes (flipping at either the blue or red defect lines). Of these, only the choice in Fig. 1, D to F, and Fig. 4, C to E, yields the **s**-tilt optical rotation. Its most interesting feature is the existence of two distinct types of PM defects: those where the handedness changes and the clinicity remains the same (drawn at the crests), and those where the handedness remains the same and the clinicity changes (drawn at the troughs). Because these defects are distinct structures, the crests and troughs of the undulation must be inequivalent, as sketched in Figs. 1, 4, and 5 and observed in the freeze-fracture experiments.

Filaments and textures. Figure 7, A to D, presents MHOBOW photomicrograph, freeze-fracture, and x-ray data that reveal the following general characteristics of the filaments, both freely suspended and grown in from the isotropic, that can be readily formed from PM phases: (i) Filaments have **s** normal or nearly normal to the filament long axis, i.e., a local structure of nested cylindrical surfaces (of circular or racetrack-shaped cross section), consistent with the layering structure proposed by Jákli *et al.* (*13*). (ii) Filaments exhibit PM layer undulation similar to that of the bulk, with **m** making an angle α(ρ) (Fig. 7C) with the local filament axis, where ρ is the distance from the filament center (*60*).

Observation (ii), coupled with the ease with which PM phases form filaments relative to non–PM phases (e.g., B2), provides strong evidence that the PM is the essential element stabilizing filament structure. PM coupled with the smectic layering forms a 2D-ordered structure analogous to that of the 2D-ordered fluid columnar phases, which are known to form freely suspended filaments (*61*, *62*). However, the extreme anisotropy of its 2D ordering makes the PM case much more interesting, as evidenced, on the one hand, by the spectacular range of possibilities (Fig. 7A), and, on the other hand, by the rigor with which a chosen structure is maintained (Figs. 2 and 7A). The latter suggests that in a growing filament, α, once chosen, is fixed. The anisotropic softness, as evidenced by the low threshold for **E**-field–induced PM suppression (*63*), enables the PM ordering to accommodate the layer curvature at the filament surface and, importantly, reduces the energy cost of helical winding of the PM undulations around and along the filament ($\alpha \sim 75°$, evident in Fig. 7C). The helical winding of the PM within the filament, with α established by a nucleation event and remaining fixed during growth (*64*), provides a natural explanation of the twist deformation of filaments. Note that with this mechanism for filament helix-

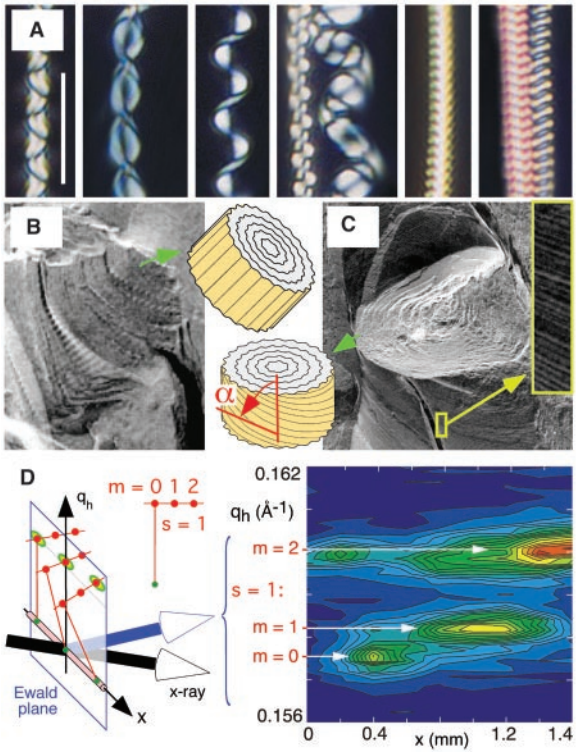

Fig. 7. Filaments and fibers. (**A**) Transmission polarized light images of different MHOBOW filaments growing within a 500-μm-by-500-μm area upon cooling a 6-μm-thick cell from the isotropic phase (scale bar, 50 μm). The twist structures are highly diverse but rigorously maintained once established, evidence of a topologically determined internal organization (*64*). (**B** and **C**) FFTEM images of MHOBOW filaments, showing the nested cylinder smectic layer organization: (B) 1-μm diameter with angle $\alpha \sim 0°$ between the filament axis and the modulation wavevector **m**, and (C) 3.4-μm diameter with $\alpha \sim 80°$. The filament helical twist is likely due to this internal helical PM winding. (**D**) X-ray scattering from a single ~30-μm-diameter freely suspended MHOBOW filament ($T = 130°C$), formed in situ by slow pulling of a pin from a 1-mm-diameter cup of LC. The x-ray beam illuminates a 0.2-mm-long segment of the filament, and the figure shows intensity contours of scans in $\mathbf{q}_h$ as a 1.4-mm length of the filament is translated through the beam parallel to its axis (x). The [s = 1, m = 0], [s = 1, m = 1], and [s = 1, m = 2] lattice points pass successively through the Ewald plane, indicative of a slightly helixed PM lattice with $\alpha \sim 0$, twisting at a rate of ~ 10°/mm along the filament, consistent with the forcing of **m** normal to the filament axis by the drawing process. α increases to ~90° as the filament thins (*60*).

ing neither relies on, nor is indicative of, net SmCP layer chirality, as is assumed in current models (*13*). Variation of filament profile (e.g., cylinder or racetrack shaped), $\alpha(\rho)$, PM and smectic elasticity, filament diameter, and filament surface energies should provide the broad parameter space necessary to account for a diverse filament morphology.

The helical filaments play a key role in the formation of the striking B7 domains observed in few-micrometer-thick cells (compare Fig. 2B and cover). The basic growth scenario is illustrated in the DTLM images of Fig. 2, which shows helical filaments in the bulk being trapped on the surface for part of their length to form focal elements. Such trapped filaments organize as folded lattices (Fig. 2B) to form birefringent 2D FCDs (Fig. 2C). A mechanism for generation of more complex textures, such as the checkerboard in Fig 2C, is shown in the parallel polarizer DTLM images in Fig. 2D, in which a filament, tethered to the surface and to the green dots (left), grows upon cooling by adding molecules all along its length (center). It spontaneously undulates, perhaps because of compressive stress due to its linear expansion, and the undulations form a 2D pattern (right) that is checkerboard or stripe-like, depending on the phase of the undulation in neighboring filaments. Such arrays internally reorganize and anneal into remarkably homogeneous periodic, quasi-periodic, or maze-like structures.

Other phases. If PM produces the structure proposed here for B7, then it may also lead to other bent-core LC phases with B7 properties. For example, the orientation frustration at the splay defect planes, instead of producing the B7 layer expansion, may be relieved by interdigitation (half-layer displacement) of the layers, which, as shown in Fig. 1H, accommodates in a natural way the opposite orientation of the bent molecules on opposite sides of a defect line. This arrangement leads directly to the 2D rectangular lattice in Fig. 1H, which is, in fact, the lattice structure of the B1 phase (*3*, *51*, *65*–*67*), identified as the "frustrated" intermediate between the B7 and the B6 phases, the latter being the lamellar structure having the "half-layer" repeat of the defect regions in Fig. 1H. The "half-layer" structure is preferred with short tails, i.e., the layering is weaker, as is the case for calamitic smectics with shorter tails (*68*). Thus, the B7-B1-B6 sequence found versus decreasing tail length in, for example, the mOAM5AMOm homologous series of bent-core dimers (*51*) may well be understood on the basis of PM. Another important example is the material W1044 (Fig. 1A), which exhibits the spectacular textures of the B7 family (*13*), but has an interdigitated 2D lattice of a phase of the B1 family (*3*, *69*).

An additional possible response to the excess layer thickness is to form layer twist grain boundaries (TGBs) at the polarization splay defect planes. Then, in the case that the splay stripes are homochiral, the twist in molecular orientation across the stripes, evident in Fig. 1H, leads to the "polarization-splayed smectic slab" TGB structure (*70*). This may be the origin of the low-birefringence optically active (dark conglomerate) textures found in MHOBOW (*10*), H87 (*9*), and other B7 materials (*71*, *72*).

Conclusion. We have presented extensive evidence that several key mysteries of fluid smectic bent-core LCs can be understood on the basis of new phases in which the local spontaneous polar/chiral ordering drives a larger scale periodic structure of polarization splay defects. The globally 2D rectangular antiferroelectric, racemic phase with splay stripes, exhibiting a striking out-of-phase alternation of polarization and chirality, is the dominant structure found in MHOBOW, the most-studied material. A basic question that remains is the extent to which this particular structure is adopted in other materials, and, for that matter, in MHOBOW, because the twist of the filaments and the varying strength of chiral response found in domains taken through the field-induced PM-uniform transition (*6*) are suggestive of net handedness. However, such observations need to be carefully interpreted because, for example, other filament-forming systems of achiral molecules exhibit macroscopic chirality as the result of a spontaneous symmetry breaking (*73*, *74*).

These findings raise a host of theoretical questions, highlighting the need for a theory of PM formation in 3D smectic phases that (i) includes the correct treatment of the smectic layer elasticity and expansion, (ii) predicts the organization of polarity and chirality, (iii) describes the PM/UL-SmCP phase transition and the effect of electric field, and (iv) enables a mechanistic understanding of the preferred splay, which is likely to be due to steric packing polarity. The organization of helical PM in the filaments with the possibility of PM TGBs (*60*) is also a fascinating defect problem, which must be attacked to develop an understanding of the filaments' diverse twisting structures. The results reveal a class of condensed phases in which polarization modulation is a dominant effect, a class based on a molecular-design theme that enables many possibilities for substitution and variation in molecular structure.

References and Notes

1. T. Niori, T. Sekine, J. Watanabe, T. Furukawa, H. Takezoe, *J. Mater. Chem.* **6**, 1231 (1996).
2. D. R. Link *et al.*, *Science* **278**, 1924 (1997).
3. G. Pelzl, S. Diele, W. Weissflog, *Adv. Mater.* **11**, 707 (1999).
4. T. Akutagawa, Y. Matsunaga, K. Yasuhara, *Liq. Cryst.* **17**, 659 (1994).
5. M. Nakata *et al.*, *Liq. Cryst.* **28**, 1301 (2001).
6. D. M. Walba *et al.*, *Science* **288**, 2181 (2000).
7. MHOBOW is a chiral molecule and is studied, unless explicitly indicated, as the racemate [(R)/(S)-MHOBOW], which behaves as if it were achiral.
8. C.-K. Lee, L.-C. Chien, *Liq. Cryst.* **26**, 609 (1999).
9. A. Eremin, S. Diele, G. Pelzl, H Nadasi, W. Weissflog, *Phys. Rev. E* **67**, 021702 (2003).
10. M. Nakata, unpublished data.
11. These materials exhibit the following B7 phase-transition temperatures (in °C) upon cooling: MHOBOW [I 139 B7 90 B4], PBCOB [I 130 B7 80 X], H87 [I 160 B7 132 B2], CITRO [I 110 B7 85 X], and 10OAM5AMO10 [I 121 B7 99 X].
12. G. Pelzl *et al.*, *Liq. Cryst.* **26**, 135 (1999).
13. A. Jákli, C. Lischka, W. Weissflog, G. Pelzl, A. Saupe, *Liq. Cryst.* **27**, 1405 (2000).
14. N. Clark, paper presented at the 17th International Liquid Crystal Conference of the International Liquid Crystal Society, Strasbourg, France, 19 to 24 July, 1998.
15. J. P. Bedel *et al.*, *Liq. Cryst.* **27**, 1411 (2000).
16. D. R. Link, N. Chattham, N. A. Clark, E. Körblova, D. M. Walba, *Bull. Am. Phys. Soc.* **44**, 1043 (1999).
17. A. Jakli, D. Kreurke, G.G. Nair, *Phys. Rev. E* **67**, 051702 (2003).
18. G. Blatter *et al.*, *Rev. Mod. Phys.* **66**, 1125 (1994).
19. S. Renn, T. Lubensky, *Phys. Rev.* **A 38**, 2132 (1988).
20. P. P. Crooker, in *Chirality in Liquid Crystals*, H. S. Kitzerow, C. Bahr, Eds. (Springer-Verlag, New York, 2001).
21. M. A. Handschy, N. A. Clark, S. T. Lagerwall, *Phys. Rev. Lett.* **51**, 471 (1983).
22. R. Kamien, J. V. Selinger, *J. Phys. Condens. Mat.* **13**, R1 (2001).
23. R. B. Meyer, P. S. Pershan, *Solid State Commun.* **13**, 989 (1973).
24. J. V. Selinger, Z.-G. Wang, R. F. Bruinsma, C. M. Knobler, *Phys. Rev. Lett.* **70,** 1139 (1993).
25. J. Pang, N. A. Clark, *Phys. Rev. Lett.* **73**, 2332 (1994).
26. G. A. Hinshaw, R. G. Petschek, R. A. Pelcovits, *Phys. Rev. Lett.* **60**, 1864 (1988).
27. G. A. Hinshaw Jr. R. G. Petschek, *Phys. Rev. A* **39**, 5914 (1989).
28. S. A. Langer, J. P. Sethna, *Phys. Rev. A* **34**, 5035 (1986).
29. I. Kraus, R. B. Meyer, *Phys. Rev. Lett.* **82**, 3815 (1999).
30. J. Pang, thesis, University of Colorado (1995); Dissertation Abstracts no. 9620652.
31. Y. Tabe, N. Shen, E. Mazur, H. Yokoyama, *Phys. Rev. Lett.* **82**, 759 (1999).
32. J. V. Selinger, R. L. B. Selinger, *Phys. Rev. E* **51**, R860 (1995).
33. J. V. Selinger, J. M. Schnur, *Phys. Rev. Lett.* **71,** 4091 (1993).
34. C.-M. Chen, T. C. Lubensky, F. C. MacKintosh, *Phys. Rev. E* **51**, 504 (1995).
35. R. B. Meyer, R. A. Pelcovits, *Phys. Rev. E* **65**, 061704 (2002).
36. T. P. Rieker *et al.*, *Phys. Rev. Lett.* **59**, 2658 (1987).
37. N. A. Clark, R. B. Meyer, *Appl. Phys. Lett.* **22**, 493 (1973).
38. XRD experiments on powder and freely suspended filament samples were carried out on the Huber four-circle goniometer on beamline X10A of the National Sychrotron Light Source at Brookhaven National Laboratory. This beamline uses a double bounce Si monochromater and a Ge 111 analyzer to obtain wavevector resolution $\delta\mathbf{q} \sim 0.0005$ Å^{-1} full width at half maximum. Powder samples were in 1-mm-diameter glass capillaries in a temperature-controlled chamber. Single-domain x-ray microbeam experiments were carried out on Microprobe Beamline BL-4A of the Photon Factory, Tsukuba, Japan, with 5-μm-thick LC samples contained between 80-μm-thick indium–tin oxide–coated glass plates. The microbeam x-ray experiment is detailed in (*39*).
39. Y. Takanishi *et al.*, *J. Mater. Chem.* **9**, 2771 (1999).
40. C.-K. Lee *et al.*, *Liq. Cryst.* **28**, 1293 (2001).
41. D. S. Shankar Rao *et al.*, *Liq. Cryst.* **28**, 1239 (2001).
42. R. Amaranatha Reddy, B. K. Sadashiva, *Liq. Cryst.* **29**, 1365 (2002).
43. D. Coleman, thesis, University of Colorado (2003).
44. Note that in the Fourier transform of $\rho(\mathbf{r})$ used to

obtain the scattered intensity $I(\mathbf{q})$, the displacement $u(\mathbf{r})$ appears in the argument of an exponential and thus enters $I(\mathbf{q})$ in a nonlinear way. Thus, with sinusoidal undulation, even though $u(\mathbf{r})$ has only the single (fundamental) harmonic, multiple diffraction orders appear versus m for $s = 1, 2$.
45. The d_m values quoted here are for fresh samples in capillaries. d_m was found to increase in time with x-ray exposure and aging at B7 temperatures (up to $d_m \sim 600$ Å in MHOBOW). This effect was particularly noticeable in freely suspended film and freeze fracture experiments, where there is more exposure to air during observation and preparation, respectively.
46. J. A. Zasadzinski, *J. Phys.* **51**, 747 (1990).
47. T. Gulik-Krzywicki, M. J. Costello, *J. Microsc.* **112**, 103 (1997).
48. Several recent papers use evidence for polarization along the layer normal in B7 phases to argue that they are simply lamellar with triclinic local layer symmetry (*9*, *49*). However, the phases in question are shown here to be undulated and polarization modulated so that the claim of triclinic behavior in a lamellar smectic may not be justified. In fact, a PM phase is triclinic essentially everywhere (wherever there is nonzero layer curvature). It may be that local triclinic symmetry actually drives the PM, but there is no evidence for this at present.
49. A. Jákli, D. Krüerke, H. Sawade, G. Heppke, *Phys. Rev. Lett.* **86**, 5715 (2001).
50. It is not understod why d_m is larger in films than in bulk, but this may be due either to surface tension, which provides an additional elastic resistance to undulation, or due to the high surface-to-volume ratio of the films, which enhances hydrolysis and impurity buildup.
51. S. W. Choi *et al.*, *Mol. Cryst. Liq. Cryst.* **328**, 185 (1999).
52. M. Nakata, N. Chattham, N. A. Clark, H. Takezoe, unpublished data.
53. C. Y. Young, R. Pindak, N. A. Clark, R. B. Meyer, *Phys. Rev. Lett.* **40**, 773 (1978).
54. The B7 materials strongly favor formation of freely suspended filaments (*12*, *16*) rather than films, a consequence of their 2D lattice structure, but it was possible to obtain 1- to 10-layer-thick MHOBOW and 10OAM5AMO10 films at high T in the B7 phase by either pulling the film very slowly (~20 μm/s) or by applying an ac field (~5 V/mm) parallel to the film plane during the pulling. An initially thin spot will expand in area over a large fraction of the film after several hours.
55. R. Pindak, C. Y. Young, R. B. Meyer, N. A. Clark, *Phys. Rev. Lett.* **45**, 1193 (1980).
56. A. Hauser, A. Schamalfuss, Kresse, *Liq. Cryst.* **27**, 629 (2000).
57. Several B7 phases have been previously identified as $SmCP_A$ on the basis of antiferroelectric properties, including absence of second-order nonlinear optical susceptibility. We contend that the underlying structure is actually SmC_SP_F and that the antiferroelectricity is that of the PM stripe pattern.
58. R. Stannarius, C. Langer, W. Weissflog. *Phys. Rev. E* **66**, 031709 (2002).
59. Because the field-induced PM/UL-to-SmCP transition is an equilibrium energetic effect, the modulation should in principle return once the field is removed. However, it did not do so spontaneously in any of the experiments reported here or in (*6*). This is likely due to the fact that in order to reach the threshold field, the LC was only 1 to 5 μm thick, and because the layer structure shrinkage upon PM expulsion was locked in by the surfaces, an effect similar to the irreversible elimination of the chevron structure in SmCs by field application. The PM/UL-to-SmCP transition in CITRO could be reversed by waveform selection (square wave: PM/UL-to-SmCP; triangle wave: SmCP -to- PM/UL) (*10*).
60. If p is the pitch of a helical winding of $\mathbf{m}(x)$ along a filament, then at radius ρ from the filament core we have $\alpha(\rho) = \rho(2\pi/p)$. Thus, if the pitch is independent of ρ, then the orientation of $\mathbf{m}$ also winds helically versus ρ at a given x and the PM lattice must have TGBs.
61. C. R. Safinya, K. S. Liang, W. A. Varady, N. A. Clark, G. Andersson, *Phys. Rev. Lett.* **53**, 1172 (1984).
62. C. R. Safinya, N. A. Clark, K. S. Liang, W. A. Varady, L. Y. Chiang, *Mol. Cryst. Liq. Cryst.* **123**, 205 (1985).
63. The elastic constant C of the PM lattice is comparable to its elastic energy density $C \sim K/d_m^2 \sim 10^4$ J/m^3 (see calculation of $\mathbf{E}_{th}$), about four orders of magnitude smaller than typical smectic layer compression moduli. Thus, the typical fluid smectic focal conic organization of layers is maintained.
64. The winding of the 2D PM lattice on a filament of fixed cross-sectional layer structure is maintained topologically by the number of undulation periods around the filament. However, the PM lattice must have dislocations because of the curvature of the smectic layers (Fig. 7, B and C).
65. J. Szydlowska *et al.*, *Phys. Rev. E* **67**, 031702 (2003).
66. The B1 lattice structure shown in Fig. 1H is one of many possibilities for alternation of polarization and tilt orientation, which also include PM in the absence of tilt. Thus, the homochiral, synpolar case (e.g., all stripe polarizations toward the reader and in magenta) would necessarity have an oblique 2D lattice, which has been found in some B1s, e.g., W1044.
67. The polarization is sketched as uniform in the B1 phase in (*53*) and the B1rev phase in (*69*), but in fact must be splayed, e.g., as in Fig. 1H.
68. W. L. McMillan, *Phys. Rev. A* **4**, 1238 (1971).
69. W1044 has an oblique 2D reciprocal lattice characterized by strong [s, m] = [1, 1] and [1, −1] reflections, with complete absence of the $s = 1$, m even reflections, indicative of an interdigitated real lattice. The real lattice is as in Fig. 1H but oblique, possibly due to a uniform rather than alternating molecular tilt orientation (*43*).
70. M. Brunet, L. Navailles, N. A. Clark, *Eur. Phys. J. E* **7**, 5 (2002).
71. A. Eremin, S. Diele, G. Pelzl, W. Weissflog, *Phys. Rev. E* **67**, 020702(R) (2003).
72. J. Ortega, C. L. Folcia, J. Etxebarria, N. Gimeno, M. B. Ros, *Phys. Rev. E* **68**, 011707 (2003).
73. B. N. Thomas, N. A. Clark, *Phys. Rev. E* **59**, 3040 (1999).
74. S. Pakhomov *et al.*, *Proc. Natl. Acad. Sci. U.S.A.* **100**, 3040 (2003).
75. This work was supported by NSF grant DMR-0072989, NSF Materials Research Science and Engineering Centers grants 0213918 (University of Colorado) and 0080034 (University of California, Santa Barbara), and NASA grant NAG3-2457. Research was carried out in part at the National Synchrotron Light Source, supported by U.S. Department of Energy, Divisions of Materials and Chemical Sciences.

Supporting Online Material

www.sciencemag.org/cgi/content/full/301/5637/1204/DC1

Figs. S1 to S3

26 March 2003; accepted 4 August 2003

Major Ecological Transitions in Wild Sunflowers Facilitated by Hybridization

Loren H. Rieseberg,[1]* Olivier Raymond,[2] David M. Rosenthal,[3] Zhao Lai,[1] Kevin Livingstone,[1] Takuya Nakazato,[1] Jennifer L. Durphy,[1] Andrea E. Schwarzbach,[4] Lisa A. Donovan,[3] Christian Lexer[1]

Hybridization is frequent in many organismal groups, but its role in adaptation is poorly understood. In sunflowers, species found in the most extreme habitats are ancient hybrids, and new gene combinations generated by hybridization are speculated to have contributed to ecological divergence. This possibility was tested through phenotypic and genomic comparisons of ancient and synthetic hybrids. Most trait differences in ancient hybrids could be recreated by complementary gene action in synthetic hybrids and were favored by selection. The same combinations of parental chromosomal segments required to generate extreme phenotypes in synthetic hybrids also occurred in ancient hybrids. Thus, hybridization facilitated ecological divergence in sunflowers.

The role of hybridization in evolution has been debated for more than a century. Two highly polarized viewpoints have emerged. At one extreme, hybridization is considered to be a potent evolutionary force that creates opportunities for adaptive evolution and speciation (*1, 2*). In this view, the increased genetic variation and new gene combinations resulting from hybridization promote the development and acquisition of novel adaptations. The contrasting position accords little evolutionary importance to hybridization (aside from allopolyploidy), viewing it as a primarily local phenomenon with only transient effects—a kind of "evolutionary noise" (*3–5*). Unfortunately, definitive support for either viewpoint is lacking. Although footprints of past hybridization are often detected by molecular phylogenetic studies (*6*), their presence does not indicate that the hybridization was adaptive. Likewise, the documentation of fit hybrids in contemporary hybrid zones (*2*) is not proof of an adaptive role for hybridization, because fit

[1]Department of Biology, Indiana University, Bloomington, IN 47405, USA. [2]Laboratoire de Biologie Moleculaire et Phytochimie, Universite Claude Bernard Lyon 1, F-69622 Villeurbanne, France. [3]Department of Plant Biology, University of Georgia, Athens, GA 30602, USA. [4]Department of Biological Sciences, Kent State University, Kent, OH 44242, USA.

*To whom correspondence should be addressed. E-mail: lriesebe@indiana.edu